On the mechanical power output comparisons of cone dielectric elastomer actuators

Chongjing Cao, Lijin Chen, Wenke Duan, Thomas L. Hill, Bo Li *Member IEEE*, Guimin Chen, Hui Li, Yingtian Li *Member IEEE*, Lei Wang *Member IEEE*, and Xing Gao

***Abstract*—The emerging demand for bio-inspired soft robotics requires novel soft actuators whose performance exceeds conventional rigid ones. Dielectric elastomer actuators (DEAs) are a promising soft actuation technology with large actuation strain and fast response. Cone DEAs are one of the most widely adopted DEA configurations for their compact structure and large force/stroke output with several configuration variations developed in recent years. By driving at a resonant frequency, the cone DEAs show a significant amplification in their power outputs, which demonstrates their suitability for highly dynamic robotic applications. However, it is still unclear how the payload conditions could affect the power outputs of cone DEAs and no work has compared the output performance of different variations of cone configurations. In this work, by considering conical configuration DEAs with generalized dissipative payloads, we conduct an extensive study on the effects of payload conditions on the power outputs of the cone DEA family. Additionally, we benchmark the performance of different cone DEA configurations and illustrate the fundamental principles behind these output patterns. The findings reported in this work establish guidelines for designing high-performance cone DEA actuators.**

***Index Terms*— Conical Configuration, Dielectric Elastomer Actuators, Power Output, Resonant Actuation, Soft Robotics**

I. Introduction

SOFT robotics is an emerging research field that seeks to develop biologically-inspired soft or partially soft robots utilizing compliant materials instead of rigid components in conventional robots. Soft robots have the potential to be more robust, adaptable and safer to interact with humans and environments [1]. The growing applications of soft robotics demand novel compliant actuation technologies beyond conventional rigid actuators. Dielectric elastomer actuators (DEAs) are promising soft actuators which possess the advantages of large actuation strains, inherent compliance and programmable actuations [2].

Despite these attractive features, early DEA designs suffered from low power outputs due to the high viscoelasticity of the elastomers [3]. To improve the power output performances of the DEAs, a resonant actuation principle has been adopted, where the DEA system is actuated at its resonance to maximize the power output, thus enabling highly dynamic applications [4] [5] [6] [7] [8] [9] [10] [11] [12] [13]. For example, a rolled DEA with the peak mass-specific power (600 W/kg) greater than natural muscles has been reported; this is able to drive a flapping wing robot to achieve tethered flight [7].

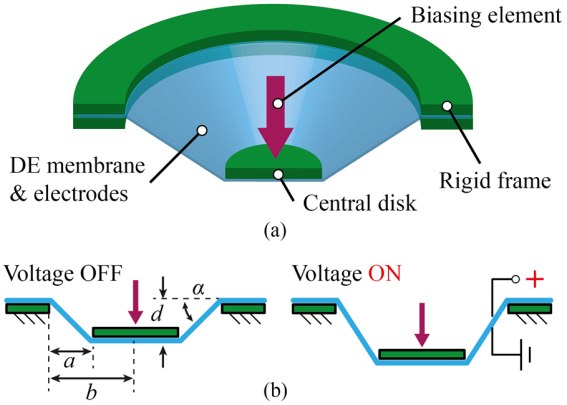

Fig. 1. Schematic diagram of (a) a cone DEA and (b) its actuation principle.

Among the DEA configurations reported in literature, conical configuration is one of the most widely adopted designs for its compact structure and large force/stroke output [14] [15] [16]. A conical configuration is achieved using a piece of dielectric elastomer bonded to a rigid frame and a central disk. A biasing element causes the membrane to deform out-of-plane, as illustrated in **Fig. 1**. The biasing element can be a linear compression spring [17], a deadweight [18], a bistable mechanism [19], permanent magnets [20], an antagonistic cone DEA membrane [14]. Many works have investigated the dynamic responses of cone DEAs [17] [18] [21] [22] [23] [24]. Hodgins *et al*. [17] and Rizzello *et al*. [18] [21] developed an electro-mechanical dynamics model for cone DEAs. Cao *et al*. investigated the effects of actuation signal components and relative phases on the nonlinear dynamic responses of a two-degree-of-freedom (DOF) cone DEA [23]. Many dynamic

Manuscript received August 21, 2020; revised xxx; accepted xxx. This work was supported in part by The National Key Research and Development Program of China under Grant 2019YFB1311600; in part by the National Natural Science Foundation of China, under Grant U1713219 and Grant 91748124. (Corresponding author: Xing Gao)

C. Cao, L. Chen, W. Duan, H. Li, Y. Li, L. Wang and X. Gao are with the Research Centre for Medical Robotics and Minimally Invasive Surgical Devices, Shenzhen Institutes of Advanced Technology (SIAT), Chinese Academy of Sciences, Shenzhen 518055, China (e-mail: cj.cao@siat.ac.cn; vendchen@outlook.com; wk.duan@siat.ac.cn; huili1@siat.ac.cn; liyingtiantj@gmail.com; wang.lei@siat.ac.cn; xing.gao@siat.ac.cn).

T. L. Hill is with the Department of Mechanical Engineering, University of Bristol, Bristol BS8 1TR, UK (e-mail: tom.hill@bristol.ac.uk).

B. Li and G. Chen are with the State Key lab of Manufacturing Systems Engineering, Shaanxi Key Lab of Intelligent Robots, School of Mechanical Engineering, Xi'an Jiaotong University, Xi'an 710049, China (e-mail: liboxjtu@xjtu.ac.cn; guimin.chen@xjtu.ac.cn).

applications that utilize cone DEAs have been developed [25] [26] [27] [28] [29] [30]. Choi and co-workers developed a series of multi-DOF cone DEA driven crawling robots [25]. Based on the resonant actuation principle, the authors proposed the first soft pneumatic pump driven by resonating cone DEAs [26].

Despite the extensive studies on its dynamics and many promising applications in the literature, relatively few works have concerned with the power outputs of cone DEAs; as such current robot designs which incorporate cone DEAs, lack systematic guidance for achieving optimal power output. In the authors' previous works, the power output of an antagonistic double cone DEA was investigated [31] [32] and it was found that, although the power output of resonant actuation may be optimized, its performance is strongly affected by the payload conditions such as the viscous dissipation and payload inertia. With the various cone DEA configurations proposed in the literature, it is essential to understand how the performance of each configuration is affected by the payload in order to determine the most suitable, and robust, design. However, the effects of dissipative payload on the power output performance of other cone DEA configurations have not previously been investigated. Furthermore, no benchmarking has been conducted to compare the power output performance of the cone DEAs. As such, there are two key questions that remain unclear. Firstly, which is the optimal cone DEA configuration for maximizing power output? Secondly, what are the fundamental mechanical principles that underpin this?

This work conducts extensive numerical and experimental studies to address these key questions. Namely, the effects of payload conditions on the power outputs of the cone DEAs are investigated to establish the fundamental principles underpinning the performance. In addition, the output performances of different cone DEA configurations are benchmarked. The rest of this paper is structured as follows. Section II introduces the cone DEA configurations to be investigated and the power output study methodology. In Section III, the power output performance of the cone DEAs is studied with a focus on the effects of the payload conditions, biasing elements and actuation signal conditions. Experimental validation is documented in Section IV. Finally, in Section V, key findings are discussed, and conclusions are drawn.

II. Comparative Model Development

A. Cone DEA configurations

This work mainly studies three different cone DEA configurations, as illustrated in **Fig. 2**. The first configuration is a Single Cone DEA with a Linear compression Spring (SCDEA-LS) [17] [21]. The payload is connected to the actuator through a rod attached to the central disk. The other two configurations involve a pair of cones formed by two pieces of DE membranes and are connected by a coupling mechanism, which are: II. a Double Cone DEA with a Rigid Rod (DCDEA-RR) [32]; III. a Double Cone DEA with a Linear compression Spring (DCDEA-LS). Note that a DCDEA-RR can be transformed such that the two central disks are attached to form an inverted double cone, as seen in [20] [33]. The inverted double cone DEA has a similar output as the DCDEA-RR due to the symmetry. Also note that, to the best of the authors' knowledge, the DCDEA-LS configuration has not been reported in previous works. Yet, it resembles a simplified version of the compliantly coupled two-DOF DEAs proposed by the authors in [34]. Also note that the three cone DEA configurations studied here represent the designs that have demonstrated resonant actuations through theoretical and experimental studies in the literature. Other configurations including cone DEAs with magnetic attraction [20] and bistable beams [19] are better suited for discrete actuations due to their inherent physical constraints such as mechanical stoppers, hence are not considered in this work. Cone DEAs with a biasing deadweight can exert continuous strokes; however, this deadweight leads to a heavy design and its working orientation is restricted, hence it is excluded from this study.

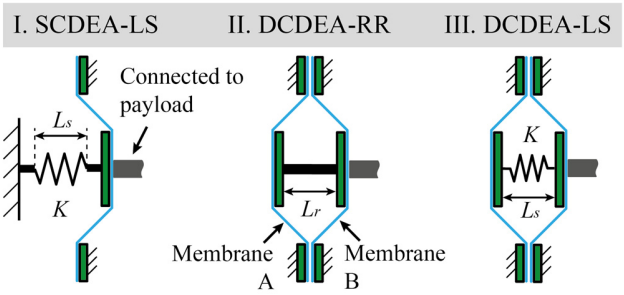

Fig. 2. Three cone DEA configurations adopted in this work.

B. Setup of power output study

This study adopts a generalized setup following the authors' previous works where a cone DEA drives an inertial and dissipative payload [31] [32], as illustrated in **Fig. 3**. This setup represents the typical dissipative payloads encountered by cone DEAs with a linear, reciprocate motion [26] [29] [32]. The actuator drives the mass, M, and a viscous dashpot, c, to move horizontally (hence gravity is neglected). Electric energy from the power source is converted to the mechanical work via the electro-mechanical coupling mechanism of the DEA.

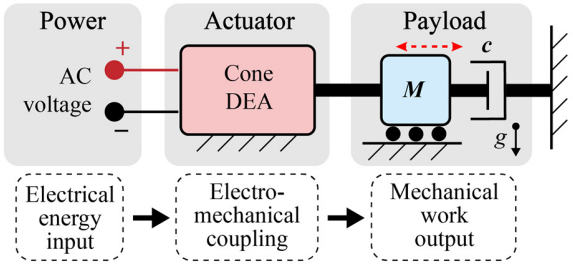

Fig. 3. Schematic illustration of the cone DEA power output study setup.

C. Model of system dynamics

Dynamic models of cone DEAs have been studied extensively in previous works, hence is described in brief here. For details regarding cone DEA modelling, please refer to these works (linear spring biasing elements: [21], rigid rod: [32]). Note that, in this work, the DEA is considered to be an elastomer membrane sandwiched between two elastomeric electrodes which have non-negligible stiffness and viscoelasticity. Although electrodes in powder or grease forms can have significantly lower stiffness thus can simplify the

modelling process, elastomeric electrodes demonstrate better reliability and a longer lifespan [35], which are favorable for practical applications. The dynamic response of the system can be fully characterized by the integration of:

i. the geometric relationship, which describes the function between the out-of-plane deformation and the radial stretch of the DEA;
ii. an electrical model that characterizes the charge flows in and out of the DEA capacitor and the actual voltage across the DE membrane;
iii. a mechanical model that estimates the reaction force of the DEA based on the inputs from the previous two modelling units, and;
iv. a dynamic model that describes the time-dependent states of the DEA-payload system.

Once the dynamic response of the system reaches a steady-state, the average power output of the DEA can be estimated. The four modelling units are introduced in the following subsections and are illustrated in **Fig. S.1**.

1) Geometric relationship

The conical configuration is constructed by deforming the DE membrane and elastomeric electrodes out-of-plane, and several simplifying assumptions are made when modelling this deformation (following [17] [21] [20] [36]) : (i) this is a single degree-of-freedom system, i.e. only translation along the longitudinal axis is considered; (ii) the deformation is truncated conical; (iii) strain distribution on the membrane/electrode is homogeneous; (iv) the circumferential deformation of the membrane/electrode does not vary.

Let a piece of DE membrane (with electrodes attached) be bonded to a rigid circular frame with the inner radius b, and a central disk with the radius a. A protrusion force, F_p, caused by the biasing element, deforms the membrane/electrode out-of-plane by a displacement d (**Fig. 1** (**b**)). Let λ_1' be the radial stretch of the membrane/electrode caused by the out-of-plane deformation and can be given by

$$\lambda_1' = \frac{\sqrt{d^2+(b-a)^2}}{(b-a)}, \tag{1}$$

The angle between the membrane/electrode and the reference plane, α, can be expressed as

$$\alpha = \sin^{-1}\frac{d}{\sqrt{d^2+(b-a)^2}}. \tag{2}$$

2) Electrical model

A DEA may be modelled as a deformable capacitor in series with two electrode resistors (assuming an ideal capacitor with no current leakage). When an input voltage is applied, and charge flows into the DEA, the charge rate and the voltage across the DEA capacitor can be expressed as

$$\dot{Q} = -\frac{1}{2R_sC}Q + \frac{1}{2R_s}\Phi_{in}, \tag{3}$$

$$\Phi_{DEA} = \frac{1}{C}Q, \tag{4}$$

where Q is the charge built on the DEA, R_s is the surface resistance of one electrode, Φ_{in} is the input voltage, Φ_{DEA} is the actual voltage across the capacitor, C is the capacitance of the DEA and is given as

$$C = \varepsilon_r\varepsilon_0\frac{\pi(b^2-a^2)}{H_m\cos\alpha}. \tag{5}$$

where ε_0 and ε_r are the absolute permittivity of a vacuum and the relative permittivity of the dielectric elastomer respectively and H_m is the membrane thickness.

3) Mechanical model

The mechanical model describes the total force exerted by the DE membrane and elastomeric electrodes along the longitudinal axis as a function of the deformation d. First, the stresses of the DE membrane and elastomeric electrodes along the radial axis need to be characterized. The stress functions for both DE membrane and elastomeric electrodes consist of hyperelastic and viscoelastic terms, where the DE membrane also has an electromechanical coupling component. Following [37], the Gent model [38] is adopted here to describe the hyperelastic stretch-stress relationship and a Maxwell rheological model is utilized to describe the viscoelasticity.

The DE membrane has an initial thickness of H_{m0} and be pre-stretched biaxially with the ratios of $\lambda_p \times \lambda_p$ before the elastomeric electrodes (thickness H_{el0}) are bonded. During the out-of-plane deformation, the total radial stretch of the DE membrane is

$$\lambda_{m1} = \lambda_1'\lambda_p, \tag{6}$$

and the radial stretch of the electrode is

$$\lambda_{el1} = \lambda_1', \tag{7}$$

The circumferential stretches of the membrane (λ_{m2}) and electrode (λ_{el2}) remain unchanged during the out-of-plane deformation (assumption (iv)), i.e. $\lambda_{m2} = \lambda_p$ and $\lambda_{el2} = 1$.

The thickness of the membrane and electrode after deformation can be written as

$$H_m = \frac{H_{m0}}{\lambda_{m1}\lambda_{m2}}, \tag{8}$$

and

$$H_{el} = \frac{H_{el0}}{\lambda_{el1}\lambda_{el2}}, \tag{9}$$

The radial stress σ_m of the DE membrane is given by

$$\sigma_m = \sigma_{m\_h} + \sigma_{m\_v} + \sigma_{m\_e}, \tag{10}$$

where σ_{m_h} is the hyperelastic stress, σ_{m_v} is the viscoelastic stress and σ_e is the electrostatic stress, and are defined as

$$\sigma_{m\_h} = \frac{\mu_{m\_A}\left(\lambda_{m1}^2-\lambda_{m1}^{-2}\lambda_{m2}^{-2}\right)}{1-\left(\lambda_{m1}^2+\lambda_{m2}^2+\lambda_{m1}^{-2}\lambda_{m2}^{-2}-3\right)/J_{m\_A}}, \tag{11.a}$$

$$\sigma_{m\_v} = \frac{\mu_{m\_B}\left(\lambda_{m1}^{e\,2}-\lambda_{m1}^{e\,-2}\lambda_{m2}^{e\,-2}\right)}{1-\left(\lambda_{m1}^{e\,2}+\lambda_{m2}^{e\,-2}+\lambda_{m1}^{e\,-2}\lambda_{m2}^{e\,-2}-3\right)/J_{m\_B}}, \tag{11.b}$$

$$\sigma_{m\_e} = -\varepsilon_0\varepsilon_r E^2, \tag{11.c}$$

where μ_{m_A} and μ_{m_B} are the shear moduli of the two springs in the Maxwell rheological model for the DE membrane, J_{m_A} and J_{m_B} are constants of the limiting stretches of the two springs, $\lambda_{m1}^e = \lambda_{m1}/\xi_{m1}$ is the stretch of the spring on the second branch in the rheological model, ξ_{m1} is the stretch of the dashpot, $\lambda_{m2}^e = 1$ based on assumption (iv), $E = \Phi_{DEA}/H_m$ is the electric field across DE membrane.

Similarly, the radial stress σ_{el} of the electrode is written as

$$\sigma_{el} = \sigma_{el\_h} + \sigma_{el\_v}, \tag{12}$$

where σ_{el_h} and σ_{el_v} are the hyperelastic and viscoelastic stresses of the electrode respectively, and are defined as

$$\sigma_{el\_h} = \frac{\mu_{el\_A}\left(\lambda_{el1}^2-\lambda_{el1}^{-2}\lambda_{el2}^{-2}\right)}{1-\left(\lambda_{el1}^2+\lambda_{el2}^2+\lambda_{el1}^{-2}\lambda_{el2}^{-2}-3\right)/J_{el\_A}}, \tag{13.a}$$

$$\sigma_{el\_v} = \tag{13.b}$$

$$\frac{\mu_{el\_B}\left(\lambda_{el1}^{e\ 2}-\lambda_{el1}^{e\ -2}\lambda_{el2}^{e\ -2}\right)}{1-\left(\lambda_{el1}^{e\ 2}+\lambda_{el2}^{e\ -2}+\lambda_{el1}^{e\ -2}\lambda_{el2}^{e\ -2}-3\right)/J_{el\_B}},$$

where μ_{el_A} and μ_{el_B} are the shear moduli of the two springs in the Maxwell rheological model for the electrode, J_{el_A} and J_{el_B} are constants of the limiting stretches of the two springs, $\lambda_{el1}^{e} = \lambda_{el1}/\xi_{el1}$ is the stretch of the spring on the second branch in the rheological model, ξ_{el1} is the stretch of the dashpot and $\lambda_{el2}^{e} = 1$.

The dashpot is modelled as a Newtonian fluid [37], and the rate of deformation of the dashpot in Eq. (11.b & 13.b) is

$$\frac{d\xi_{m1}}{\xi_{m1}dt} = \frac{1}{3\eta_m}\left(\frac{\mu_{m\_B}\left(\lambda_{m1}^{e\ 2}-\lambda_{m1}^{e\ -2}\lambda_{m2}^{e\ -2}\right)}{1-\left(\lambda_{m1}^{e\ 2}+\lambda_{m2}^{e\ 2}+\lambda_{m1}^{e\ -2}\lambda_{m2}^{e\ -2}-3\right)/J_{m\_B}} - \frac{\mu_{m\_B}\left(\lambda_{m2}^{e\ 2}-\lambda_{m1}^{e\ -2}\lambda_{m2}^{e\ -2}\right)/2}{1-\left(\lambda_{m1}^{e\ 2}+\lambda_{m2}^{e\ 2}+\lambda_{m1}^{e\ -2}\lambda_{m2}^{e\ -2}-3\right)/J_{m\_B}}\right), \quad (14.a)$$

$$\frac{d\xi_{el1}}{\xi_{el1}dt} = \frac{1}{3\eta_{el}}\left(\frac{\mu_{el\_B}\left(\lambda_{el1}^{e\ 2}-\lambda_{el1}^{e\ -2}\lambda_{el2}^{e\ -2}\right)}{1-\left(\lambda_{el1}^{e\ 2}+\lambda_{el2}^{e\ 2}+\lambda_{el1}^{e\ -2}\lambda_{el2}^{e\ -2}-3\right)/J_{el\_B}} - \frac{\mu_{el\_B}\left(\lambda_{el2}^{e\ 2}-\lambda_{el1}^{e\ -2}\lambda_{el2}^{e\ -2}\right)/2}{1-\left(\lambda_{el1}^{e\ 2}+\lambda_{el2}^{e\ 2}+\lambda_{el1}^{e\ -2}\lambda_{el2}^{e\ -2}-3\right)/J_{el\_B}}\right), \quad (14.b)$$

where η_m and η_{el} are the viscosity of the dashpot for the DE membrane and electrode model respectively.

Then the total force of the DE membrane along the longitudinal axis can be given by

$$F_{DEA} = -2\pi a H_m \sigma_m \sin\alpha - 2\times 2\pi a H_{el}\sigma_{el}\sin\alpha\ . \quad (15)$$

4) Dynamics model

The equation of motion for a single cone DEA-payload system is given by

$$(m+M)\ddot{d} + c\dot{d} - F_{DEA} = F_p\ , \quad (16)$$

where m is the mass of the central disk (neglecting the mass of the membrane).

The system states of the single cone DEA-payload system are described by the deformation, d, velocity, $\dot{d}$, stretches of the dashpots in the rheological model, ξ_{m1} and ξ_{el1}, and charge accumulated on the DEA, Q.

For double cone DEA systems, let d_A and d_B be the deformation of membrane A and membrane B (i.e. the membrane connected to the payload) respectively. Note that for the DCDEA-RR, the system has 1-DOF, d_A and d_B must fulfill $d_A = d_B - L_r$, where L_r is the length of the coupling rod. The equation of motion can be written

$$(2m+M)\ddot{d}_B + c\dot{d}_B - F_{DEA\_A} = F_{DEA\_B}\ , \quad (17)$$

where $F_{DEA\_A,B}$ are the forces exerted by membranes A and B.

For the DCDEA-LS configuration with 2-DOF, the equations of motion are given by

$$m\ddot{d}_A - F_{DEA\_A} = -F_p\ , \quad (18.a)$$

$$(m+M)\ddot{d}_B + c\dot{d}_B - F_{DEA\_B} = F_p\ . \quad (18.b)$$

The expression for the force, F_p, is listed in **Table S.I**.

5) Performance characterization

The complete system model consists of the geometric relationship, electrical model, mechanical model and the mechanical dynamics model that were described in the previous subsections. With the input voltage(s) pre-defined, and the initial conditions given, the states of the DEA-payload system can be estimated by integrating the equation(s) of motion numerically in time domain. Once the system response reaches a steady-state, the average mechanical power output of the DEA can be estimated by

$$P_{out} = \frac{1}{T}\int_0^T f(v)v\,dt\ , \quad (19)$$

where T is the period, v is the velocity of the payload ($v = \dot{d}$ in 1-DOF systems and $v = \dot{d}_B$ in 2-DOF systems), t is time and $f(v) = cv$ is the linear viscous damping function.

It is worth noting that the linear viscous dashpot is a simplified representation of the dissipative factors in real systems. The different dissipation forces such as nonlinear viscous damping (aerodynamic load) or Coulomb damping (friction) in real systems can be considered by replacing the damping term, $f(v)$, in Eq. (19) by the more complex damping functions, allowing a comparison to be drawn with the setup considered in this work.

The average electrical power input is

$$P_{in} = \frac{1}{T}\sum\int_0^T \Phi_{in} i\,dt\ , \quad (20)$$

where the summation symbol represents the total power input if both membranes are actuated for the double cone configurations.

Note that in this study, no electrical energy recovery is included, i.e. charge flowing back into the power supply is not considered. As such, the electro-mechanical efficiency is

$$\eta_{em} = \frac{P_{out}}{P_{in}}\ . \quad (21)$$

D. Parameter identification and model validation

To ensure a fair comparison of the output performance, the parameters of each biasing element are tuned to ensure the same out-of-plane deformation of d_0 = 4 mm (for DCDEAs, membrane A is deformed by d_0 = -4 mm due to the symmetry in the configurations). For the two linear spring configurations SCDEA-LS and DCDEA-LS, the spring constant is also fixed at k = 600 N/m. The radius of the central disk and the support frame are set at a = 7.5 mm and b = 15 mm respectively.

ELASTOSIL 2030 silicone film with the thickness of 100 μm (Wacker Chemie AG) is adopted as the DE membrane material for its low viscoelasticity. A mixture of carbon black power (20%w.t.) and ELASTOSIL RT 625 was pad-printed on both sides of the DE membrane as the elastomeric electrodes. The thickness of the pad-printed electrodes was measured by a stylus profiler (DektakXT, BRUKER) to have a mean thickness of 8 μm and the surface resistance was measured at 100 kΩ (LCR meter, E4980AL, Keysight). Further details of the DEA fabrication process are reported in the Supplementary Material.

Experiments were conducted to identify the parameter values and to validate the model. First, a force-displacement test was performed to identify the quasi-static model parameters. A linear rail (X-LSQ150B-E01, ZABER) was adopted to deform the center of the DEA at a constant velocity of 0.025 mm/s while a load cell (S/N 835827, FUTEK) was used to measure the reaction force. Next, a frequency sweep was performed to

investigate the dynamic response of the DEAs. A varying-frequency sinusoidal voltage signal (at 1 Hz/s) was generated by MATLAB and applied to the DEA via a high voltage amplifier (10/40A-HS, TREK). A laser displacement sensor (LK-G152 and LKGD500, Keyence) was used to measure the DEA response at a sampling rate of 20 kHz. The experimental setups for quasi-static and dynamic tests are shown in **Fig. 4**.

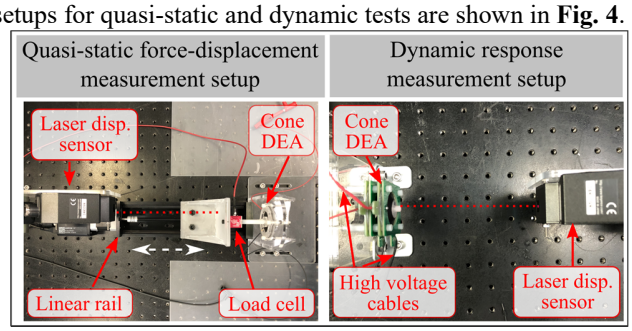

Fig. 4. Force-displacement and dynamic response experimental setups.

The quasi-static experimental results are shown in **Fig. 5 (a)**, while **Fig. 5 (b)** is the forward frequency sweep results (0 - 160 Hz) for a SCDEA-LS. The model parameters were determined by fitting the experimental results using a least-mean-squared algorithm in MATLAB (following [17] [18]) and are listed in **Table S.II**. As can be seen in **Fig. 5**, the model developed in this work agrees well the experimental results.

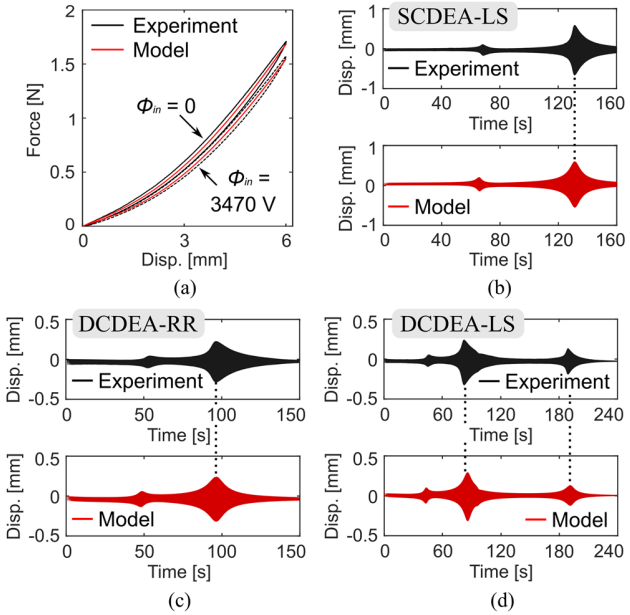

Fig. 5. (a) Quasi-static force-displacement experimental results and model predictions. (b-d) Frequency responses of the SCDEA-LS, DCDEA-RR and DCDEA-LS respectively.

III. Output Performance Comparison

In this section, the power output of cone DEAs with various payload conditions is investigated. The payload mass, M, and damping coefficient, c, are varied from 0.1-10 g and 0.1-10 N.s/m respectively and, for each payload combination [M, c], a numerical simulation is conducted by adopting a forward frequency step from 1 to 200 Hz with a step size of 0.2 Hz. At each frequency, 100 actuation cycles are repeated to ensure a steady-state system response; the last five cycles are used for mean power output estimation. The maximum power output under this payload condition, P_{max}, is the peak value of the mean power in the frequency domain. A square wave with an amplitude of 4.9 kV is used to actuate the DEA, which is equivalent to a nominal electric field of 80 MV/m. Note that, to achieve a fair comparison between single and double cone DEAs, an actuation voltage is applied to only one membrane for the DCDEAs. The cases where both membranes are actuated are investigated in Section III.*C*. Membrane A in the DCDEA-RR is actuated, since both membranes are physically constrained to deform with the payload synchronously, actuating either membrane would lead to an identical result. However, for the DCDEA-LS, only membrane B is in direct contact with the payload, hence actuating membrane B will lead to a direct drive of the payload, which is similar to the other two configurations. However, actuating membrane A changes the driving method to an indirect drive, which could perform differently. For this, we compare the output performances of the DCDEA-LS when actuating membrane A/B in this study.

A. Results overview

The amplitudes and the power outputs (P_{out}) against the actuation frequency for each configuration are plotted in **Fig. 6**. The payload condition is M = 0.1 g and c = 0.1 N.s/m in all four examples. Note from **Fig. 6** that, in all cases, the maximum power output of the actuator closely corresponds to its resonance, demonstrating the clear advantage of using a resonant actuation strategy. The maximum power output of each cone DEA configuration is compared to the payload mass, M, and damping coefficient, c, in **Fig. 7**. It can be noted that, for all cone DEA configurations investigated in this work, the damping plays a critical role in their maximum power outputs, while the payload mass shows a minor effect on P_{max}. For the SCDEA-LS, DCDEA-RR and DCDEA-LS with direct driving (membrane B actuated, DCDEA-LS B), their P_{max} values drop sharply with an increase in damping. Note that, the P_{max} values for the DCDEA-RR and DCDEA-LS B are lower than the SCDEA-LS since the antagonistic membrane serves as an additional damper which reduces the outputs.

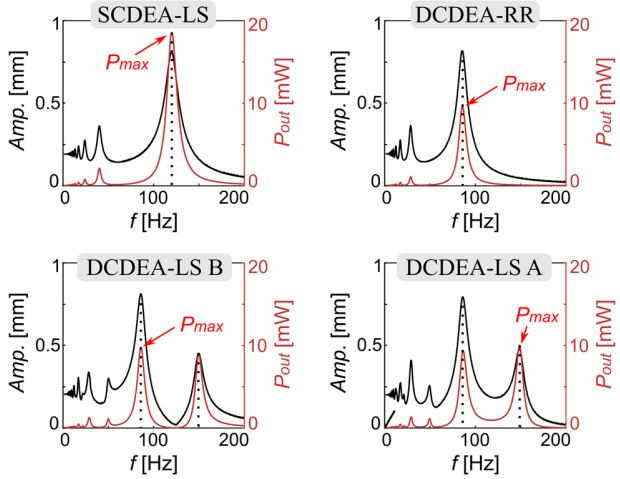

Fig. 6. Actuator amplitudes and power outputs against the actuation frequency of the SCDEA-LS, the DCDEA-RR, the DCDEA-LS with membrane B actuated, and the DCDEA-LS with membrane A actuated.

It is worth noting from **Fig. 7**, that the DCDEA-LS incorporating indirect driving (membrane A actuated, DCDEA-

LS A) shows a completely different trend against the payload compared to the other cases. Its maximum power output rises with the increasing damping before maintaining at a consistently high value. At the highest damping coefficient of c = 10 N.s/m, its P_{max} is still over 18 mW, which is more than 20-fold higher than the other direct drive cases.

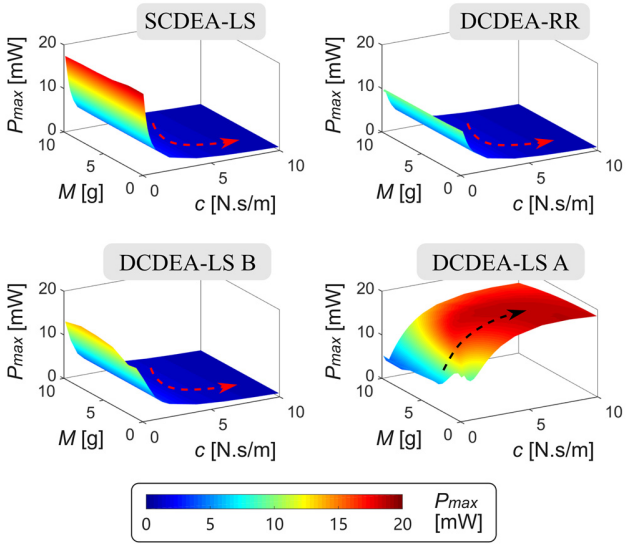

Fig. 7. Maximum power outputs against the payload damping coefficient, c, and mass, M, of the SCDEA-LS configuration, the DCDEA-RR with a single membrane actuated, the DCDEA-LS with membrane B actuated (direct drive), and the DCDEA-LS with membrane A actuated (indirect drive).

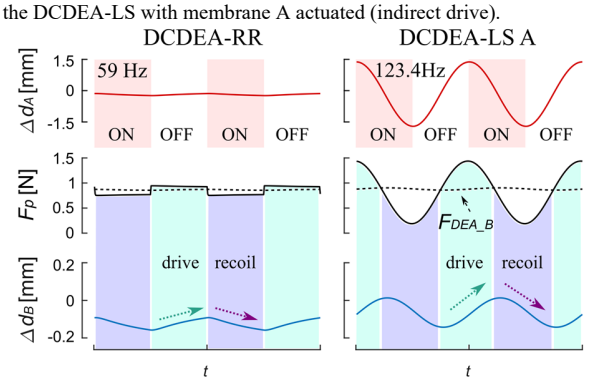

Fig. 8. Time histories of the membrane displacements and the force balances of the DCDEA-RR and DCDEA-LS A when their power outputs reach the maxima. The payload parameters are M = 2 g and c = 10 N.s/m.

The fundamental mechanical principle behind the high-power outputs of the DCDEA-LS in highly damped conditions lies in its compliant coupling mechanism. **Fig. 8** compares the time histories of the membrane displacements and the protrusion force, F_p, of the DCDEA-RR and DCDEA-LS A when they reach their maximum power for the payload condition of M = 2 g and c = 10 N.s/m. The dashed line illustrates the force exerted by membrane B. The difference between F_p and F_{DEA_B} is the driving force for the dissipative payload. As illustrated in **Fig. 8**, when F_p is larger than F_{DEA_B}, membrane B together with the payload is driven towards its maximum displacement, then in the second half of the cycle, the recoil force of membrane B moves the payload back to its minimum displacement. It can be noted from the response phase that, when the payload damping is high, resonant actuation is no longer adopted by the rigidly coupled DCDEA-RR for maximizing its power output. The displacements are approximately in-phase with the actuation voltage, and the driving force is a result of the electrostatic force change in membrane A, which leads to a low power output. However, due to the additional DOF introduced in the DCDEA-LS, where the driving membrane A is not in direct contact with the highly damped payload, it is able to maintain a high amplitude resonant actuation while pumping much higher power to the payload than the DCDEA-RR.

B. Effects of payload damping

In the previous subsection, the maximum power output of the four DEA configurations were compared to the payload conditions. It was found that, despite the decrease in the resonant frequency caused by the increase of the payload mass, an increase in mass has a minor effect on the power outputs. It is the payload damping that greatly affects the cone DEA's power output. Hence, in this subsection, the influence of the payload damping on the power outputs are investigated, while fixing the payload mass at M = 2 g.

Fig. 9 shows the power outputs and electro-mechanical efficiencies of the three cone DEA configurations as a function of actuation frequency and damping coefficient. It can be noted that, for the two 1 DOF configurations (SCDEA-LS and DCDEA-RR), in lightly damped conditions, the power output and the electro-mechanical efficiency first increase with the frequency from below resonance, and reach their peaks before drop to low values. The peak power output and electro-mechanical efficiency reduce sharply as c > 1 N.s/m. On the other hand, for the 2-DOF DCDEA-LS A configuration, in light damping conditions (c < 0.5 N.s/m), a local P_{out} maximum of 6.3 mW occurs near 70 Hz, while the global maximum of 18.7 mW appears near 130 Hz. The two power output maxima are correlated to the resonance of the two modes in the 2-DOF system. As c increases, the first local maximum vanishes quickly and the global maximum remains at a high value. This is believed to be due to the change in the amplitudes and phases of the two underlying linear modes of the system as c increases [39], which alters the responses of the two membranes. Note that, despite having the highest P_{max} value among all configurations, the efficiency, η_{max}, is relatively low due to the higher power consumption.

C. Effects of double-membrane actuation

In the previous subsections, only one DE membrane is actuated for the DCDEA configurations. However, it is more common for DCDEAs to actuate both membranes to increase the total stroke output. Here the power output performance of DCDEAs, with both membranes actuated, is investigated and benchmarked against the single-actuation counterpart for each configuration. For the DCDEA-RR, the two actuation signals are restricted to antiphase to achieve antagonistic actuation, however, due to the compliant coupling mechanism, the DCDEA-LS allows voltage signals with relative phases from 0 to 2π [23]. As a result, in this study, both antiphase and in-phase actuation voltages in the DCDEA-LS will be analyzed.

The maximum power outputs for the DCDEA-RR with antiphase voltages, and the DCDEA-LS with both antiphase and in-phase voltages are shown in **Fig. 10** (**a-c**) respectively and their comparisons against the single-actuation results are illustrated in **Fig. 10** (**d-f**) respectively. The P_{max} ratio is defined as the ratio between the P_{max} values in the double- and single-actuation cases under the same payload condition. It can be noted from **Fig. 10** (**a**) that, similar to the single-actuation counterpart, the DCDEA-RR shows a clear decrease in its power output with the increasing c. However, the power output performance demonstrates a significant improvement of about 4-fold compared to the single-actuation counterpart.

The maximum power output of the DCDEA-LS with antiphase voltage signals occurs when $c < 1$ N.s/m (**Fig. 10** (**b**)). At higher damping ratios, a rapid reduction in P_{max} is seen, before a slight increase to a steady value. By comparing the P_{max} ratio in **Fig. 10** (**e**), a surprising result can be noticed: apart from the light damping conditions, antiphase actuation voltages result in a slightly lower power output than the single-actuation counterpart under the same payload conditions. By benchmarking the DCDEA-LS with in-phase voltage signals against the single-actuation counterpart demonstrates that notable improvements are only achieved for light damping and mass conditions, while in the other payload conditions, its maximum power outputs are similar.

Intuitively, a double-actuated DCDEA could exert a higher power output than a single-actuated one as the energy gained by the system every cycle is doubled (for the equivalent response amplitude and frequency). However, the reduced performance of the double-actuation DCDEA-LS requires further investigation beyond the highly abstracted maximum power output maps shown in **Fig. 10**. **Fig. 11** plots the power output and efficiency against damping in the frequency domain for the three cases in **Fig. 10** with M fixed at 2 g.

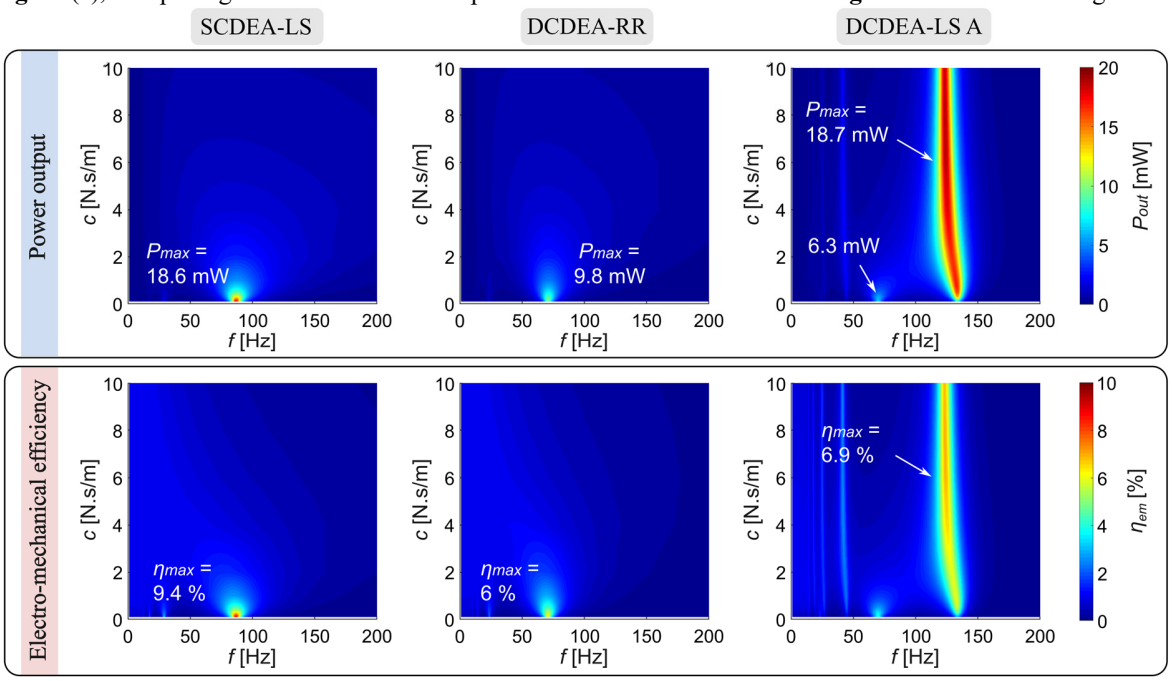

Fig. 9. Power output and electro-mechanical efficiency of the cone DEA configurations as a function of actuation frequency and payload damping.

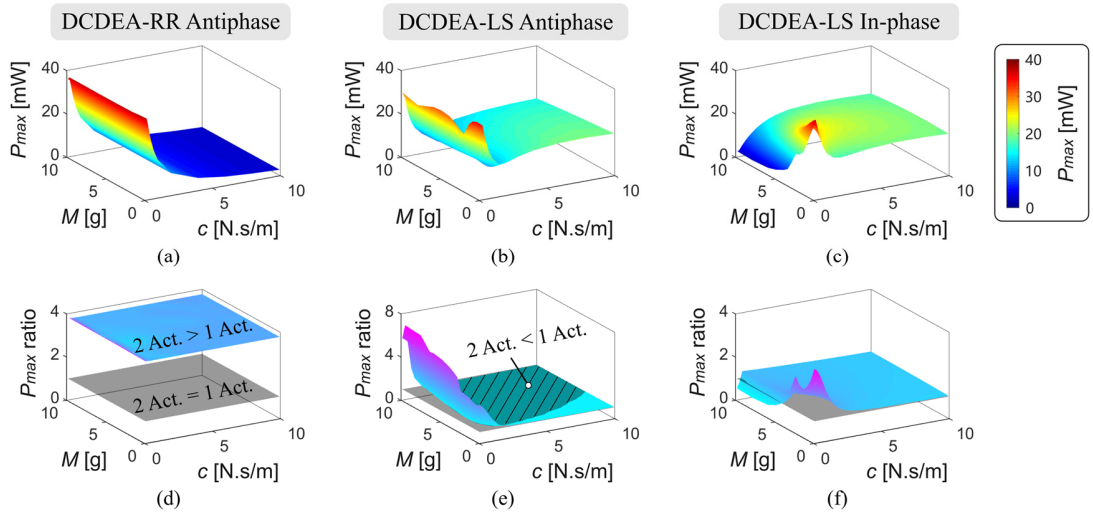

Fig. 10. Maximum power output against payload conditions and the benchmark comparison against the single-actuation counterparts for: (a & d) the DCDEA-RR with antiphase voltage signals; (b & e) the DCDEA-LS with antiphase voltage signals, and; (c & f) the DCDEA-LS with in-phase voltage signals

It can be noted from **Fig. 11** that, antagonistic actuation dramatically boosts the maximum power output and the efficiency of the DCDEA-RR compared to the single-actuation results shown in **Fig. 9**. It has the highest P_{max} and η_{max} among the three cases. For a DCDEA-LS with antiphase actuation voltages, the maximum power output occurs at two different frequency regions for different damping coefficients. When the damping is relatively light (c < 2 N.s/m), the P_{max} occurs near the 1st linear natural frequency of the system, as the actuation signals are mainly forcing the system in its 1st mode. A lower power peak also occurs near the 2nd linear natural frequency where the responses are antiphase. As the damping increases, it causes the change in the amplitudes and phases of the two underlying modes [39], which leads to a change in the oscillation amplitudes and relative phase between the two membranes. The power output peak near the 1st linear natural frequency decreases rapidly while the power peak corresponding to the 2nd linear natural frequency increases. When the forcing in the DCDEA-LS becomes in-phase, the resonant response is dominated by the 2nd mode, and a peak power output of 30 mW is obtained using the in-phase forcing in a light damping condition. The maximum power output rises with the increasing damping before gradually decreasing.

In all three excitation cases, as the oscillation amplitude of membrane B reduces with the increasing c, the power output by membrane B also reduces (see the direct driving cases in **Fig. 7** for examples), while membrane A gradually becomes the dominant driving unit. As a result, regardless of the actuation amplitude and phase for membrane B, the DCDEA-LS shows a close power output performance in high damping conditions for all three cases. With twice the power consumption, the electro-mechanical efficiencies for the double-actuation DCDEA-LS in high damping conditions are much lower than the single-actuation counterpart.

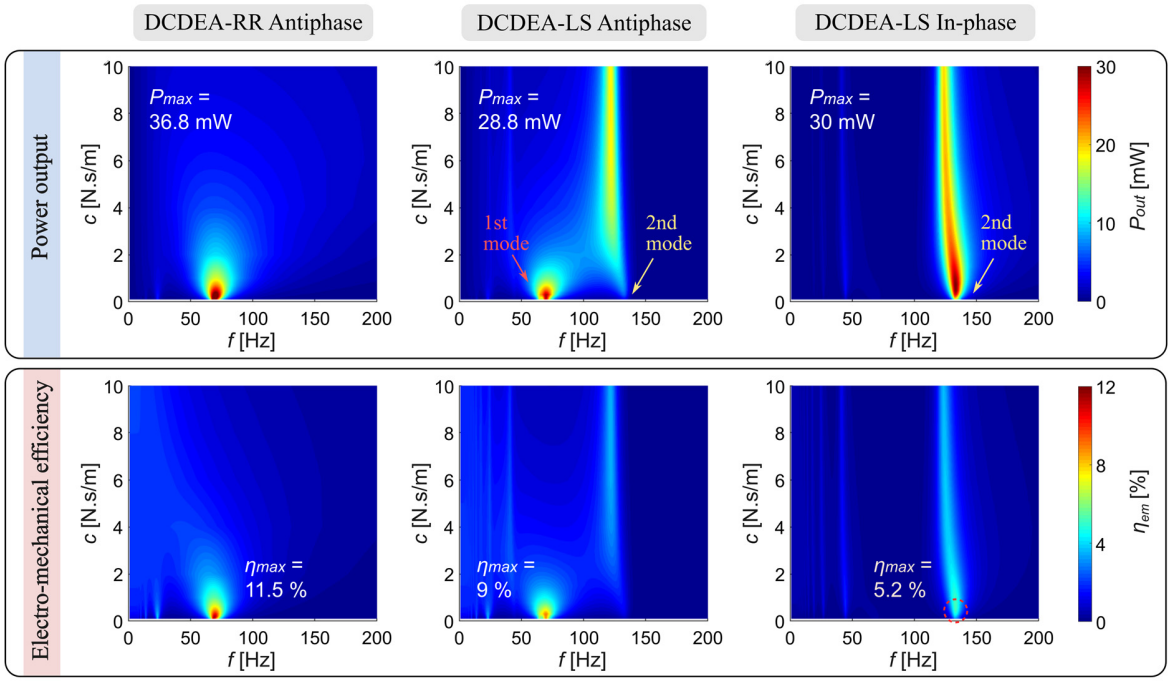

Fig. 11. Power output and electro-mechanical efficiency of the double cone DEA configurations as a function of actuation frequency and payload damping with both membranes actuated.

IV. Experimental Validation

In Section III, the power output study results showed a strong correlation between the payload damping and the power output, and the key findings are summarized as follows:

1. In single membrane actuation cases:

a) For low payload damping conditions, the SCDEA-LS has a higher power output than the DCDEA-RR and DCDEA-LS while the DCDEA-LS has the lowest power output;

b) For high payload damping conditions, the DCDEA-LS (indirect drive) has the highest power output.

2. In double membrane actuation cases:

a) For low payload damping conditions, the DCDEA-RR with antiphase voltages has a higher power output than the DCDEA-LS with both anti- and in-phase actuation voltages;

b) For high payload damping conditions, the DCDEA-LS with in-phase voltages shows the highest power output.

This section describes experiments that were conducted to verify these key findings. An example of the output experimental setup for the SCDEA-LS configuration is plotted in **Fig. 12**, where the DCDEA-RR and DCDEA-LS tests also follow the similar setup. A Nylon rod (with M = 1.65 g) represents the payload, with on end attached to the central disk of the DEA and the other end submerged in a viscous fluid. The lightweight Nylon rod minimizes the effects of gravity and ensures the experiments are representative of the theoretical study. The DEA drives the Nylon rod to oscillate in the fluid, where the hydrodynamic drag serves as the damping of the payload system. The viscous fluid adopted in this work is a solution of methyl cellulose (CAS: 9004-67-5, aladdin) in water, which is commonly adopted for tuning the Reynolds number in

fluid dynamic studies [40]. By varying the concentration of the methyl cellulose, the dynamic viscosity of the solution can be adjusted to simulate different payload damping values. Eight different solutions were prepared and, using a viscometer, were confirmed to have dynamic viscosities of 1, 100, 300, 10^3, 3×10^3, 10^4, 3×10^4, and 10^5 mPa.s. To find the maximum output of the DEAs in different dynamic viscosity conditions, a discrete frequency step was performed from 1 to 200 Hz with the step size of 0.2 Hz, 50 cycles of excitation signals were repeated at each frequency to ensure the DEA reached a steady-state response. The displacement of the payload was measured by a laser displacement sensor at the sampling rate of 20 kHz. The measured displacement data was then processed in MATLAB to obtain the root-mean-square (RMS) velocity for each frequency. Recall from Eq. (19) that, the average power output for the DEA is a function of its RMS velocity V_{RMS}; therefore, instead of calculating the exact power output (which involves complex fluid dynamics), we may directly compare the V_{RMS} value as a representation of the actuator's power output. The maximum V_{RMS} in the frequency domain represents the peak power output of the DEA for a given viscosity condition. For each DEA configuration, three DEA samples were tested, and the results were averaged.

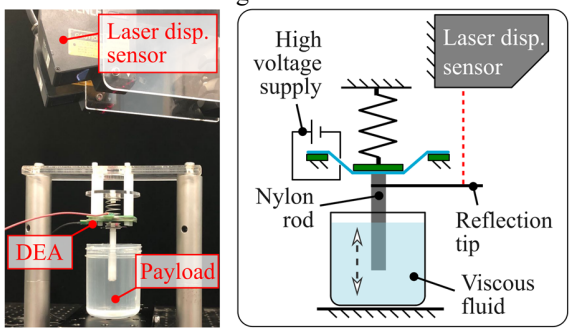

Fig. 12. Photo and schematic illustration of the power output study experimental setup.

Fig. 13 (a) plots the maximum V_{RMS} of each configuration with different dynamic viscosities. It can be noted that, when the dynamic viscosity is at the lowest value, the SCDEA-LS has the highest V_{RMS}, hence power output, among the three configurations with one membrane actuated (black curves). Meanwhile, the DCDEA-RR configuration, with two membranes actuated antagonistically, shows the highest V_{RMS} value amongst three double-actuation cases (red and green curves). These two results agree with the theoretical findings 1 a) and 2 a) respectively. For the DCDEA-LS configuration, as the dynamic viscosity increases, the V_{RMS} values for the antiphase double-actuation case (red curve) and single-actuation direct drive case (black curve) decrease much faster than the single-actuation indirect drive case (blue curve), and show poorer performances than the single-actuation case when the viscosity is increased. This result was also verified by the theoretical study shown in **Fig. 10 (e)**. **Fig. 13 (b)** compares the V_{RMS} for the three configurations at the highest viscosity of 10^5 mPa.s. As reported in the findings 1 b) and 2 b), the DCDEA-LS A (indirect drive) demonstrates the highest V_{RMS}, hence power output, in the single-actuation case and the DCDEA-LS with in-phase double-actuation shows the best performance of the three double-actuation cases. All the experimental results agree very well with the theoretical conclusions in this work.

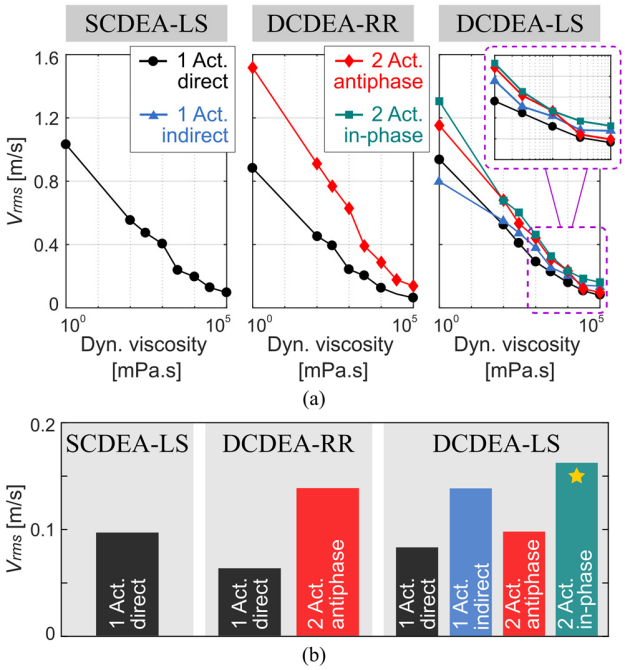

Fig. 13. Power output study experimental results. (a) Measured RMS output velocities against the payload dynamic viscosity for three configurations. (b) Comparison of the V_{RMS} at the highest dynamic viscosity of 10^5 mPa.s

V. Conclusion

In this work, a comprehensive study was conducted on the power output performances of three cone DEA configurations that incorporate the resonant actuation principle. The effects of dissipative payloads on the power output performance of the cone DEAs were investigated and the output performances of different cone DEA configurations were benchmarked.

The power study results illustrated that the DCDEA-LS shows the highest robustness against the payload damping, which is the major factor that affects the output of the other cone configurations. The compliant coupling mechanism of the DCDEA-LS enables resonance of the driving DE membrane while transferring high power output to the payload.

Cone DEAs are one of the most widely adopted DEA configurations and have applications in soft robotic locomotion, vibration isolation and fluidic devices. Yet the high dissipative payload conditions, for instance the aerodynamic drag in the flapping wing robot [32] and the hydraulic force in the underwater swimming robot [29], dramatically reduces the maximum power output of conventional cone DEAs (e.g. DCDEA-RR & SCDEA-LS), hence limits the performance of such devices. The novel compliantly coupled configuration (DCDEA-LS) proposed in this work is a promising candidate for improving the performance of cone DEA based soft robotic devices. For example, in a recent work by the authors, the first resonant cone DEA driven soft pneumatic pump has been developed, by adopting the compliant coupling principle [26].

With the advances in the high-performance DE and electrode materials and onboard power electronics, it is anticipated that cone DEAs incorporating the complaint coupling principle will

have broad applications in soft robotics such as surveillance, environment monitoring and biomedical devices.

The novel findings reported in this work could offer valuable guidelines for designing high-performance cone DEA actuators and dynamic DEA applications. The power output study setup developed here can be readily adopted for conducting analyses and optimizations on various DEA configurations.

REFERENCES

[1] D. Rus and M. T. Tolley, "Design, fabrication and control of soft robots," *Nature*, vol. 521, no. 7553, pp. 467–475, 2015, doi: 10.1038/nature14543.

[2] R. Pelrine, R. Kornbluh, Q. Pei, and J. Joseph, "High-speed electrically actuated elastomers with strain greater than 100%," *Science (80-.).*, vol. 287, no. 5454, pp. 836–839, 2000, doi: 10.1126/science.287.5454.836.

[3] J.-P. L. Lucking Bigué and J.-S. Plante, "Experimental Study of Dielectric Elastomer Actuator Energy Conversion Efficiency," *IEEE/ASME Trans. Mechatronics*, vol. 18, no. 1, pp. 169–177, 2013, doi: 10.1109/TMECH.2011.2164930.

[4] W. Kaal and S. Herold, "Electroactive polymer actuators in dynamic applications," *IEEE/ASME Trans. Mechatronics*, vol. 16, no. 1, pp. 24–32, 2011, doi: 10.1109/TMECH.2010.2089529.

[5] R. Sarban, B. Lassen, and M. Willatzen, "Dynamic electromechanical modeling of dielectric elastomer actuators with metallic electrodes," *IEEE/ASME Trans. Mechatronics*, vol. 17, no. 5, pp. 960–967, 2012, doi: 10.1109/TMECH.2011.2150239.

[6] H. Zhao, A. M. Hussain, M. Duduta, D. M. Vogt, R. J. Wood, and D. R. Clarke, "Compact Dielectric Elastomer Linear Actuators," *Adv. Funct. Mater.*, vol. 28, no. 42, p. 1804328, 2018, doi: 10.1002/adfm.201804328.

[7] Y. Chen *et al.*, "Controlled flight of a microrobot powered by soft artificial muscles," *Nature*, vol. 575, 2019, doi: 10.1038/s41586-019-1737-7.

[8] C. Tang, B. Li, H. Fang, Z. Li, and H. Chen, "A speedy, amphibian, robotic cube: Resonance actuation by a dielectric elastomer," *Sensors Actuators, A Phys.*, vol. 270, pp. 1–7, 2018, doi: 10.1016/j.sna.2017.12.003.

[9] T. Li *et al.*, "Fast-moving soft electronic fish," *Sci. Adv.*, vol. 3, no. 4, pp. 1–8, 2017, doi: 10.1126/sciadv.1602045.

[10] G. Gu, J. Zou, R. Zhao, X. Zhao, and X. Zhu, "Soft wall-climbing robots," *Sci. Robot.*, vol. 3, no. 25, p. eaat2874, 2018, doi: 10.1126/scirobotics.aat2874.

[11] X. Ji *et al.*, "An autonomous untethered fast soft robotic insect driven by low-voltage dielectric elastomer actuators," *Sci. Robot.*, vol. 4, p. eaaz6451, 2019.

[12] W. Li, W. Zhang, H. Zou, Z. Peng, and G. Meng, "A Fast Rolling Soft Robot Driven by Dielectric Elastomer," *IEEE/ASME Trans. Mechatronics Trans. Mechatronics*, vol. 23, no. 4, pp. 1630–1640, 2018, doi: 10.1109/TMECH.2018.2840688.

[13] U. Gupta, Y. Wang, H. Ren, and J. Zhu, "Dynamic modeling and feedforward control of jaw movements driven by viscoelastic artificial muscles," *IEEE/ASME Trans. Mechatronics*, vol. 24, no. 1, pp. 25–35, 2019, doi: 10.1109/TMECH.2018.2875521.

[14] A. T. Conn and J. Rossiter, "Towards holonomic electro-elastomer actuators with six degrees of freedom," *Smart Mater. Struct.*, vol. 21, no. 3, p. 035012, 2012, doi: 10.1088/0964-1726/21/3/035012.

[15] S. Hau, G. Rizzello, and S. Seelecke, "A novel dielectric elastomer membrane actuator concept for high-force applications," *Extrem. Mech. Lett.*, vol. 23, pp. 24–28, 2018, doi: 10.1016/j.eml.2018.07.002.

[16] S. Hau, A. York, G. Rizzello, and S. Seelecke, "Performance prediction and scaling laws of circular dielectric elastomer membrane actuators," *J. Mech. Des.*, vol. 140, no. 11, p. 113501, 2018, doi: 10.1115/1.4039104.

[17] M. Hodgins, G. Rizzello, D. Naso, A. York, and S. Seelecke, "An electro-mechanically coupled model for the dynamic behavior of a dielectric electro-active polymer actuator," *Smart Mater. Struct.*, vol. 23, no. 10, p. 104006, 2014, doi: 10.1088/0964-1726/23/10/104006.

[18] G. Rizzello, M. Hodgins, D. Naso, A. York, and S. Seelecke, "Dynamic Modeling and Experimental Validation of an Annular Dielectric Elastomer Actuator With a Biasing Mass," *J. Vib. Acoust.*, vol. 137, no. 1, p. 011005, 2015, doi: 10.1115/1.4028456.

[19] M. Hodgins, A. York, and S. Seelecke, "Experimental comparison of bias elements for out-of-plane DEAP actuator system," *Smart Mater. Struct.*, vol. 22, no. 9, p. 094016, 2013, doi: 10.1088/0964-1726/22/9/094016.

[20] X. Li, W. Li, W. Zhang, H. Zou, Z. Peng, and G. Meng, "Magnetic force induced tristability for dielectric elastomer actuators," *Smart Mater. Struct.*, vol. 26, no. 10, p. 105007, 2017, doi: 10.1088/1361-665X/aa8282.

[21] G. Rizzello, M. Hodgins, D. Naso, A. York, and S. Seelecke, "Modeling of the effects of the electrical dynamics on the electromechanical response of a DEAP circular actuator with a mass-spring load," *Smart Mater. Struct.*, vol. 24, no. 9, p. 094003, 2015, doi: 10.1088/0964-1726/24/9/094003.

[22] J. Zou, G. Y. Gu, and L. M. Zhu, "Open-loop control of creep and vibration in dielectric elastomer actuators with phenomenological models," *IEEE/ASME Trans. Mechatronics*, vol. 22, no. 1, pp. 51–58, 2017, doi: 10.1109/TMECH.2016.2591069.

[23] C. Cao, T. L. Hill, A. T. Conn, B. Li, and X. Gao, "Nonlinear Dynamics of a Magnetically Coupled Dielectric Elastomer Actuator," *Phys. Rev. Appl.*, vol. 12, no. 4, p. 044033, 2019, doi: 10.1103/PhysRevApplied.12.044033.

[24] Z. Ye and Z. Chen, "Modeling and control of a 2-DOF dielectric elastomer diaphragm actuator," *IEEE/ASME Trans. Mechatronics*, vol. 24, no. 1, pp. 218–227, 2019, doi: 10.1109/TMECH.2019.2890864.

[25] H. Jung, P. T. Hoang, H. Phung, T. D. Nguyen, C. T. Nguyen, and H. R. Choi, "Development of an Insect-Inspired Hexapod Robot Actuated by Soft Actuators," *J. Mech. Robot.*, vol. 10, no. 6, p. 061016, 2018, doi: 10.1115/1.4041258.

[26] C. Cao, X. Gao, and A. T. Conn, "A Magnetically Coupled Dielectric Elastomer Pump for Soft Robotics," *Adv. Mater. Technol.*, vol. 4, no. 8, p. 1900128, 2019, doi: 10.1002/admt.201900128.

[27] Y. Zhao, Q. Guo, S. Wu, G. Meng, and W. Zhang, "Design and experimental validation of an annular dielectric elastomer actuator for active vibration isolation," *Mech. Syst. Signal Process.*, vol. 134, p. 106367, 2019, doi: 10.1016/j.ymssp.2019.106367.

[28] P. Linnebach, F. Simone, G. Rizzello, and S. Seelecke, "Development, manufacturing, and validation of a dielectric elastomer membrane actuator–driven contactor," *J. Intell. Mater. Syst. Struct.*, vol. 30, no. 4, pp. 636–648, 2019, doi: 10.1177/1045389X18818778.

[29] C. Tang, W. Ma, B. Li, M. Jin, and H. Chen, "Cephalopod-Inspired Swimming Robot Using Dielectric Elastomer Synthetic Jet Actuator," *Adv. Eng. Mater.*, vol. 1901130, p. 1901130, 2019, doi: 10.1002/adem.201901130.

[30] P. Linnebach, G. Rizzello, S. Seelecke, and S. Seelecke, "Design and validation of a dielectric elastomer membrane actuator driven pneumatic pump," *Smart Mater. Struct.*, vol. 29, no. 7, p. 075021, 2020, doi: 10.1088/1361-665X/ab8a01.

[31] C. Cao, X. Gao, and A. T. Conn, "Towards efficient elastic actuation in bio-inspired robotics using dielectric elastomer artificial muscles," *Smart Mater. Struct.*, 2019.

[32] C. Cao, X. Gao, S. Burgess, and A. T. Conn, "Power optimization of a conical dielectric elastomer actuator for resonant robotic systems," *Extrem. Mech. Lett.*, vol. 35, p. 100619, 2020, doi: 10.1016/j.eml.2019.100619.

[33] C. Cao, R. S. Diteesawat, J. Rossiter, and A. T. Conn, "A Reconfigurable Crawling Robot Driven by Electroactive Artificial Muscle," in *2019 2nd IEEE International Conference on Soft Robotics (RoboSoft)*, 2019, pp. 840–845.

[34] C. Cao, X. Gao, and A. T. Conn, "A compliantly coupled dielectric elastomer actuator using magnetic repulsion," *Appl. Phys. Lett.*, vol. 114, no. 1, p. 011904, 2019, doi: 10.1063/1.5071439.

[35] S. Rosset and H. R. Shea, "Flexible and stretchable electrodes for dielectric elastomer actuators," *Appl. Phys. A Mater. Sci. Process.*, vol. 110, no. 2, pp. 281–307, 2013, doi: 10.1007/s00339-012-7402-8.

[36] G. Berselli, R. Vertechy, G. Vassura, and V. Parenti-Castelli, "Optimal synthesis of conically shaped dielectric elastomer linear actuators: Design methodology and experimental validation,"

IEEE/ASME Trans. Mechatronics, vol. 16, no. 1, pp. 67–79, 2011, doi: 10.1109/TMECH.2010.2090664.
[37] C. Chiang Foo, S. Cai, S. Jin Adrian Koh, S. Bauer, and Z. Suo, "Model of dissipative dielectric elastomers," *J. Appl. Phys.*, vol. 111, no. 3, p. 034102, 2012, doi: 10.1063/1.3680878.
[38] A. . Gent, "A New Constitutive Relation for Rubber," *Rubber Chem. Technol.*, vol. 69, no. 1, pp. 59–61, 1996.
[39] D. Wagg and S. Neild, *Nonlinear vibration with control*. Dordrecht, 2009.
[40] K. M. Digumarti, A. T. Conn, and J. Rossiter, "Eumobot: Replicating euglenoid movement in a soft robot," *J. R. Soc. Interface*, vol. 15, no. 148, p. 20180301, 2018, doi: 10.1098/rsif.2018.0301.

Chongjing Cao was awarded the Ph.D. in robotics and autonomous systems from University of Bristol, UK, in 2019.
He is now with the Shenzhen Institutes of Advanced Technology, Chinese Academy of Sciences where he is a postdoc researcher. His research interests include bio-inspired robotic systems and the dynamics of soft actuators.

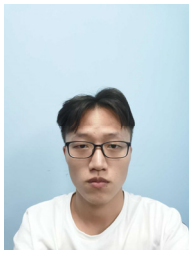

Lijin Chen received his B.S. degree in mechanical engineering from Tianjin University of Technology, China, in 2019. He is currently working toward his M.S. degree at Wuhan University of Technology, China. His research interests involve electro-active polymers.

Wenke Duan received the M.Eng. degree in mechanical engineering from Wuyi University, Jiangmen, China, in 2016. He is now a mechanical engineer with the Shenzhen Institutes of Advanced Technology, Chinese Academy of Sciences, China, with interests in surgical robotics.

Thomas L. Hill received his Ph.D. in mechanical engineering from University of Bristol, UK, in 2015. He is now a lecturer in Mechanical Engineering Department at University of Bristol since 2017.
His research interests include nonlinear modelling, nonlinear modal interactions, and nonlinear system identification.

Bo Li was awarded his Ph.D. degree in instrumental science and technology from Xi'an Jiaotong University, Xi'an, China, in 2012.
He is currently an associate professor at Xi'an Jiaotong University. He is the Associate Editor for IEEE Transaction on Automation Sciences and Engineering.

Guimin Chen received B.S., M.S., Ph.D. from the School of Mechatronics Engineering of Xidian University in 2000, 2003 and 2005. He is now a full professor at Xi'an Jiaotong University and the dean of institute of intelligent robots. He is the Associate Editor of ASME Journal of Mechanisms and Robotics.

Hui Li received his Ph.D. in Mechanical Engineering from the University of Kentucky, USA in 2014. Currently, he is an associate professor at Shenzhen Institutes of Advanced Technology, Chinese Academy of Sciences, Shenzhen, China. His research interests include Flexible Sensors and Flexible MEMS.

Yingtian Li received his M.Sc. and Ph.D. degrees in Mechanical Engineering from the University of Hong Kong in 2013 and 2018 respectively. He is currently an Associate Professor in the Shenzhen Institutes of Advanced Technology (SIAT), Chinese Academy of Sciences, China. His research interests include medical robotics, soft robots, and continuum robots.

Lei Wang received the Ph.D. in biomedical engineering in 2000. He is now with the Shenzhen Institutes of Advanced Technology, Chinese Academy of Sciences, as a Professor and the Research Director with the Institute of Biomedical and Health Engineering. Dr. Wang's research interests focus on Wearable Body Sensor Networks.

Xing Gao received his M.Sc. and Ph.D. degrees in mechanical engineering from Loughborough University, UK in 2012 and 2016, respectively. He is currently an Associate Professor at Research Centre for Medical Robotics and Minimally Invasive Surgical Devices, Shenzhen Institutes of Advanced Technology, Chinese Academy of Sciences. His research interests include smart materials and soft robotics.